

A Novel Ternary Evolving Estimator for Positioning Unmanned Aerial Vehicle in Harsh Environments

Kaiwen Xiong, Sijia Chen, Wei Dong

Abstract—Obtaining reliable position estimation is fundamental for unmanned aerial vehicles during mission execution, especially in harsh environments. But environmental interference and abrupt changes usually degrade measurement reliability, leading to estimation divergence. To address this, existing works explore adaptive adjustment of sensor confidence. Unfortunately, existing methods typically lack synchronous evaluation of estimation precision, thereby rendering adjustments sensitive to abnormal data and susceptible to divergence. To tackle this issue, we propose a novel ternary-channel adaptive evolving estimator equipped with an online error monitor, where the ternary channels, states, noise covariance matrices and especially aerial drag, evolve simultaneously with environment. Firstly, an augmented filter is employed to pre-processes multidimensional data, followed by an inverse-Wishart smoother utilized to obtain posterior states and covariance matrices. Error propagation relation during estimation is analysed and hence an indicator is devised for online monitoring estimation errors. Under this premise, several restrictions are applied to suppress potential divergence led by interference. Additionally, considering motion dynamics, aerial drag matrix is reformulated based on updated states and covariance matrices. Finally, the observability, numerical sensitivity and arithmetic complexity of the proposed estimator are mathematically analyzed. Extensive experiments are conducted in both common and harsh environments (with average RMSE 0.17m and 0.39m respectively) to verify adaptability of algorithm and effectiveness of restriction design, which shows our method significantly outperforms the state-of-the-art.

Index Terms—Position Estimation, Harsh Environments, Adaptive Noise Covariance, Aerial Drag Estimation

I. INTRODUCTION

UNMANNED aerial vehicles (UAVs) are increasingly employed to replace manpower in harsh environments [1]. To achieving autonomous execution and efficient operation, high-precision positioning and navigation are urgently demanded [2]–[4]. Unfortunately, in challenging scenarios such as cave exploration [5], facilities maintenance [6], etc, sensor interference and rapid environmental changes underscore the need for further refinement of positioning methods.

Typically, to achieve high-precision positioning, many works leverage peripheral equipment including GNSS [7], [8], motion capture system [9], pre-established beacon system [10] and assistant robot [11]. However, GNSS navigation turns out infeasible for obstruction of signal in many researches [12],

Kaiwen Xiong, Sijia Chen and Wei Dong are with the State Key Laboratory of Mechanical System and Vibration, School of Mechanical Engineering, Shanghai Jiaotong University, Shanghai, 200240, China. Corresponding author: Wei Dong, E-mail: dr.dongwei@sjtu.edu.cn.

Manuscript received Month xx, 2xxx; revised Month xx, xxxx; accepted Month x, xxxx.

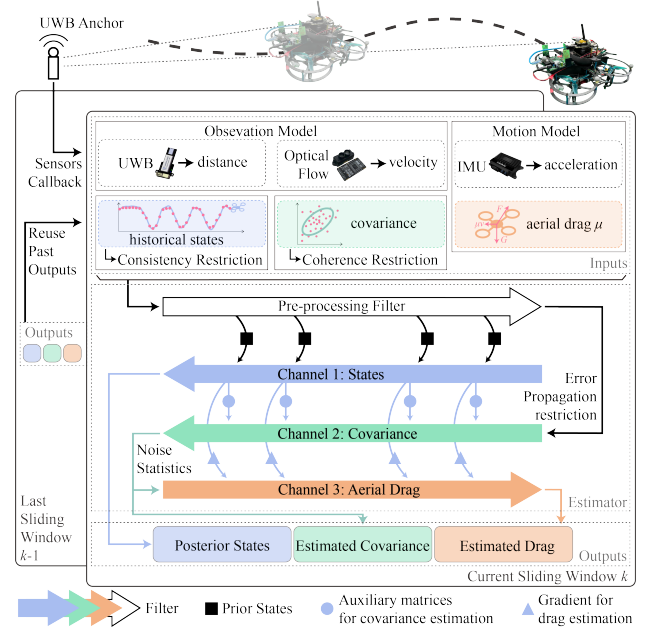


Fig. 1. An overview of proposed method TEE.

[13], while deploying additional peripheral equipment may be limited by resource constraints in numerous applications. Hence onboard sensors have garnered significant interest. Two primary categories of them include visual odometry (VO), which encompasses cameras [14], [15] and lidar [16], albeit requiring substantial computational resources. The alternative category comprises non-visual methods such as ultra-wideband radio (UWB) [17], [18], laser [19], and inertial measurement units (IMU), which usually have limited information and inadequate positioning precision in complex situations. Under this premise, integrated systems like UWB-VO [20] or visual-inertial odometry [21], [22] effectively mitigate drawbacks from both categories. To handle environmental interference and achieve better positioning precision, it's critical to distinguish varying degrees of sensor failure and properly exploit return data according to sensor reliability.

Adaptive algorithms are developed to tackle this issue. They concurrently estimates states and noise's statistical properties based on optimal estimators such as maximum a posteriori (MAP), Kalman filter (KF) [23] and sliding window filter [24]. Among various methods, one category is empirical adjustment incorporating deliberately designed factors [25] and fuzzy system [26], [27]. The second category explores statistical approaches such as exploiting sample covariance [28], moment

estimation with forgetting factor [29]–[32]. The third category employs modeling with prior distributions, such as Student’s t -distribution [33] and inverse-Wishart distribution [34], [35]. The forementioned methods demonstrate their competence in slowly changing environments. However, in challenging scenarios, current estimators fail to synchronously assess estimation error, rendering them susceptible to faulty data due to sensor interference. Furthermore, these estimators struggle to adapt to sudden environmental changes, which diminishes estimation precision and increases risk of potential divergence.

Furthermore, the variability in aerial drag presents another facet of environmental change. Studies indicate that accounting for aerial drag is crucial in the motion modeling of UAVs [36], significantly enhancing the precision of position estimation [37], [38]. The adaptive method for drag effect of ground vehicle has been studied [39], but for UAV, ought to complexity of aerodynamics, it deserves further research.

To address above issues, we elaborately develop a novel method called *ternary evolving estimator (TEE)*, which operates across three interconnected channels: state estimation, covariance matrix adaptation, and particularly aerial drag effects, as is illustrated in Fig. 1. Compared to the state-of-the-arts, we design an online error inspector, and accordingly introduce several restrictions to decide when to and how much to adjust. Initially, to pre-processes multi-dimensional data, we conduct an augmented Kalman filter within overlapping sliding windows, which is enhanced with coherence restriction to inherit historical information and consistency restriction to maintain numerical stability. Subsequently, processed data undergo a backward smoother yielding posterior states which are utilized to help covariance and drag estimation evolve with changeable interference. Notably, error propagation restriction is included to mitigate impact of abrupt environmental changes on estimation accuracy. Finally, estimation of the aerial drag matrix leverages gradient descent method based on estimated states, and those covariance matrices are used in return to determine evolving speed. These interconnected channels are conducted successively. All outputs of ternary channels are reused as inputs at next timestep.

For sensor configuration, we employ IMU and optical flow sensor to compensate for limited operation range and single data dimension of UWB. Conversely, mitigates the error accumulation of IMU and potential degradation in vision of the optical flow sensor. This synergistic approach enhances system robustness against environmental changes and interference. Moreover, we mathematically analyse essential properties including observability, stability, numerical sensitivity and arithmetic complexity. Numerous experiments are performed to support these analyses and demonstrate the adaptability of the proposed method. Additionally, we design various ablation experiments to validate effectiveness of each design.

The major contributions of our work are threefold: 1) We propose an augmented sliding window Kalman filter that balances precision with computational efficiency by leveraging sufficient data. 2) We elaborately design an error propagation matrix as an online error inspector to assess estimation performance, and accordingly develop an restricted inverse-Wishart smoother to derive posterior states and adjust noise

covariance synchronously. 3) We construct a novel aerial drag estimator via gradient descent method to enhance estimation performance, which is based on estimated states and restricted by noise statistics.

II. PRELIMINARIES

A. Notations

In this article, an m by n matrix, $\mathbf{A} \in \mathbb{R}^{m \times n}$, is referred by capital bold letter, whereas vector of dimension n , $\mathbf{x} \in \mathbb{R}^n$, is denoted by lowercase bold character. Identity and zero matrix of dimension $m \times n$ are represented as $\mathbf{I}_{m \times n}$ and $\mathbf{0}_{m \times n}$ respectively, and to simplify, the square ones of size n are abbreviated as \mathbf{I}_n and $\mathbf{0}_n$ respectively. If their dimension is not emphasized, the index will be omitted. The transposition and inverse of matrix (\cdot) are $(\cdot)^T$ and $(\cdot)^{-1}$ respectively. Also, prior and posterior quantities usually are decorated with superscripts, $(\cdot)^{\circ}$ and $(\cdot)^{\hat{\circ}}$ respectively. Commonly, a quantity with index, $(\cdot)_k$, indicates it is at timestep k , and for brevity, $(\cdot)_{1:k}$ means a series of vectors (\cdot) ’s within the timestep range from 0 to K , which is equivalent to $[(\cdot)_1^T, (\cdot)_2^T, \dots, (\cdot)_K^T]^T$. Other less common symbols will be elucidated the first time they are encountered.

B. Basic Concepts

In this work, we consider a discrete-time, linear and time-varying model as follows:

$$\text{process model: } \mathbf{x}_k = \mathbf{A}_{k-1}\mathbf{x}_{k-1} + \mathbf{u}_k + \mathbf{w}_k \quad (1a)$$

$$\text{observation model: } \mathbf{y}_k = \mathbf{C}_k\mathbf{x}_k + \mathbf{n}_k \quad (1b)$$

where k is the discrete-time index with its maximum K . The state vector $\mathbf{x}_k = [\mathbf{p}_k^T, \mathbf{v}_k^T]^T \in \mathbb{R}^6$ consists of 3-dimensional position and velocity, which are the focus of our estimation. The measurements from sensor system is $\mathbf{y}_k \in \mathbb{R}^m$, where m is the size of it. The transition matrix $\mathbf{A}_{k-1} \in \mathbb{R}^{6 \times 6}$ and the observation matrix $\mathbf{C}_k \in \mathbb{R}^{m \times 6}$ are already known based on historical knowledge. The net input is \mathbf{u}_k , and it is also written as $\mathbf{u}_k = \mathbf{B}_k\mathbf{i}_k$, where $\mathbf{B}_k \in \mathbb{R}^{6 \times n}$ is a known control matrix and $\mathbf{i}_k \in \mathbb{R}^n$ is the original input of size n .

The processing and observation noises are formulated as unbiased Gaussian distribution, i.e. $\mathbf{w}_k \sim \mathbf{N}(\mathbf{0}, \mathbf{Q}_k)$ and $\mathbf{n}_k \sim \mathbf{N}(\mathbf{0}, \mathbf{R}_k)$. Also, they are assumed to be uncorrelated:

$$\mathbb{E}[\mathbf{w}_i\mathbf{w}_j^T] = \begin{cases} \mathbf{0} & , i \neq j \\ \mathbf{Q}_i & , i = j \end{cases} \quad (2a)$$

$$\mathbb{E}[\mathbf{n}_i\mathbf{n}_j^T] = \begin{cases} \mathbf{0} & , i \neq j \\ \mathbf{R}_i & , i = j \end{cases} \quad (2b)$$

$$\mathbb{E}[\mathbf{w}_i\mathbf{n}_j^T] = \mathbf{0} \quad (2c)$$

where $\mathbb{E}[\cdot]$ denotes the mathematical expectation. And $\mathbf{N}(\boldsymbol{\mu}, \boldsymbol{\Sigma})$ represents multivariate Gaussian distribution (a.k.a. normal distribution) with PDF:

$$\mathbf{N}(\mathbf{x}; \boldsymbol{\mu}, \boldsymbol{\Sigma}) = \frac{\exp\left(-\frac{1}{2}(\mathbf{x} - \boldsymbol{\mu})^T \boldsymbol{\Sigma}^{-1}(\mathbf{x} - \boldsymbol{\mu})\right)}{\sqrt{(2\pi)^k |\boldsymbol{\Sigma}|}} \quad (3)$$

where the \mathbf{x} in front of semicolon is k -dimensional random variable, whereas $\boldsymbol{\mu}$ and $\boldsymbol{\Sigma}$ after semicolon are mean and

covariance parameters respectively. The determinant is represented as $|\cdot|$ and exponent based on natural constant e is denoted by $\exp(\cdot)$. Also in our work, the state \mathbf{x}_k is assumed to be Gaussian, i.e. $\mathbf{x}_k \sim \mathbf{N}(\check{\mathbf{x}}, \check{\mathbf{P}})$ or $\mathbf{x}_k \sim \mathbf{N}(\hat{\mathbf{x}}, \hat{\mathbf{P}})$.

In statistics, the inverse-Wishart distribution is commonly considered as a conjugate prior for the covariance parameter of a multivariate Gaussian distribution with PDF as follows:

$$\mathbf{IW}(\mathbf{C}; \sigma, \Sigma) = \frac{|\Sigma|^{\frac{\sigma}{2}} |\mathbf{C}|^{-\frac{\sigma+n+1}{2}} \exp\left(-\frac{1}{2}\text{tr}(\Sigma\mathbf{C}^{-1})\right)}{2^{\frac{\sigma n}{2}} \Gamma_n\left(\frac{\sigma}{2}\right)} \quad (4)$$

where the random variable \mathbf{C} and the scale matrix Σ are $n \times n$ positive-definite matrices. The $\Gamma_n(\cdot)$ means n -dimensional multivariate gamma function and the σ is the degree of freedom parameter.

III. METHODOLOGY

A. Motion and Observation Models

Various interference from harsh environments poses a daunting challenge on sensor configuration. Practical application requires both light-weighting and resilience to interference. Under this premise, we deliberately design a sensor system consisting of single UWB anchor, IMU and optical flow sensor. We only use one pre-deployed anchor, while IMU and optical flow sensor are onboard lightweight equipment, which indicates its convenience in practical application. Also, different working condition for each chosen sensor guarantees that single kind of interference, such as dim light or long distance, only affects certain sensor and leaves the others safe to function well. The components are explained as follows.

The IMU collects normalized linear acceleration $\mathbf{a} = [a_x, a_y, a_z]^T$ and normalized quaternion $\mathbf{q} = [q_w, q_x, q_y, q_z]^T$. The rotation matrix is obtained by:

$$\mathbf{R} = 2 \begin{bmatrix} \frac{1}{2} - q_y^2 - q_z^2 & q_x q_y - q_w q_z & q_x q_z + q_w q_y \\ q_x q_y + q_w q_z & \frac{1}{2} - q_x^2 - q_z^2 & q_y q_z - q_w q_x \\ q_x q_z - q_w q_y & q_y q_z + q_w q_x & \frac{1}{2} - q_x^2 - q_y^2 \end{bmatrix} \quad (5)$$

where $\mathbf{R} \in \text{SO}(3)$ is a member of the special orthogonal Lie group. Since the original output acceleration is also normalized, we should take the following step to obtain the net acceleration:

$$\mathbf{i} = g\mathbf{R}\mathbf{a} + [0, 0, -g]^T \quad (6)$$

where $g \simeq 9.8$ is gravitational acceleration. By pre-integration, the motion model is formulated as follows:

$$\begin{aligned} \mathbf{x}_k &= \begin{bmatrix} \mathbf{I}_3 & dt \cdot \mathbf{I}_3 \\ \mathbf{0}_3 & \mathbf{I}_3 - dt \cdot \boldsymbol{\mu} \end{bmatrix} \mathbf{x}_{k-1} + \begin{bmatrix} \frac{1}{2} dt^2 \\ dt \end{bmatrix} \otimes \mathbf{i}_k \\ &= \mathbf{A}_{k-1} \mathbf{x}_{k-1} + \mathbf{u}_k \end{aligned} \quad (7)$$

where \otimes is Kronecker product and dt is the time between timestep $k-1$ and k .

Remark 1: The $\boldsymbol{\mu} \in \mathbb{R}^{3 \times 3}$ is aerial drag matrix. It will be discussed thoroughly in Subsection III-D, but before that it is assumed already known.

With the help of IMU and the above assumption, environmental interference won't affect our motion model. This helps to maintain stability for a long time even though all

measurements fail temporarily, which suggests its robustness in harsh environments.

Typically, UWB is a non-linear sensor. For the computational efficiency, it is linearized by:

$${}^{\text{UWB}}y_k = \begin{bmatrix} \frac{\tilde{\mathbf{p}}_k^T}{\|\tilde{\mathbf{p}}_k\|_2} & \mathbf{0}_{1 \times 3} \end{bmatrix} \mathbf{x}_k \quad (8)$$

where $\|\cdot\|_2$ is the 2-norm (a.k.a. Euclidean norm). The $\tilde{\mathbf{p}}_k$ is an approximate position calculated via (7):

$$\tilde{\mathbf{p}}_k = [\mathbf{I}_3 \quad \mathbf{0}_3] (\mathbf{A}_{k-1} \check{\mathbf{x}}_{k-1} + \mathbf{u}_k) \quad (9)$$

where $\check{\mathbf{x}}_{k-1}$ is the output of the last sliding window, and thereby it is known here.

The UWB applies a global constraint on our estimator, which suppresses the error accumulation and overcomes the most common interference, vision degradation.

Remark 2: For convenience, we set the origin at the same place as UWB anchor. But in practical application, since UWB anchor is fixed w.r.t. world frame, its position can be pre-calibrated easily. If we choose different origin, by subtracting UWB's position \mathbf{p}_{UWB} from both sides of (9) and adding $\tilde{\mathbf{p}}_k^T \mathbf{p}_{\text{UWB}} / \|\tilde{\mathbf{p}}_k\|_2$ to ${}^{\text{UWB}}y_k$, it achieves the same effect as (8).

The optical flow sensor measures velocity, which have no range limitation, and this compensates for the disadvantage of UWB. Typically, optical flow method only obtains 2-dimensional velocity, which is horizontal velocity here. By calculating the difference of height obtained from a laser unit between each timestep, we gain the vertical velocity. The observation model is formulated as follows:

$$\mathbf{y}_k = \begin{bmatrix} {}^{\text{UWB}}y_k \\ {}^{\text{OF}}y_k \end{bmatrix} = \begin{bmatrix} \frac{\tilde{\mathbf{p}}_k^T}{\|\tilde{\mathbf{p}}_k\|_2} & \mathbf{0}_{1 \times 3} \\ \mathbf{0}_3 & \mathbf{I}_3 \end{bmatrix} \mathbf{x}_k = \mathbf{C}_k \mathbf{x}_k. \quad (10)$$

The advantage of this system is that the position and velocity parts of observation model compensate for weaknesses of each other, which guarantees the robustness of measurements and enhances the adaptability in changeable environments.

B. Augmented Sliding Window Kalman Filter

This part is the basis of TEE, which pre-processes all information collected by sensors and data calculated previously by TEE itself. We exert Kalman filter (KF) during a sliding window. And since every sliding window overlaps each other, we redundantly calculate the posterior state at each timestep many times, as is displayed in Fig. 2. To fully exploit this redundancy, we use an interesting trick to consider our KF itself as some other kind of sensors. Thus, the measurements as well as corresponding observation and covariance matrices are augmented as follows:

$$\tilde{\mathbf{y}}_j = \begin{cases} [\mathbf{y}_j^T, \check{\mathbf{x}}_j^T]^T, & j = 1, 2, \dots, k_w - 1 \\ \mathbf{y}_j, & j = k_w \end{cases} \quad (11a)$$

$$\tilde{\mathbf{C}}_j = \begin{cases} [\mathbf{C}_j^T, \mathbf{I}_6]^T, & j = 1, 2, \dots, k_w - 1 \\ \mathbf{C}_j, & j = k_w \end{cases} \quad (11b)$$

$$\tilde{\mathbf{R}}_j = \begin{cases} \text{diag}(\mathbf{R}_j, \check{\mathbf{P}}_j), & j = 1, 2, \dots, k_w - 1 \\ \mathbf{R}_j, & j = k_w \end{cases} \quad (11c)$$

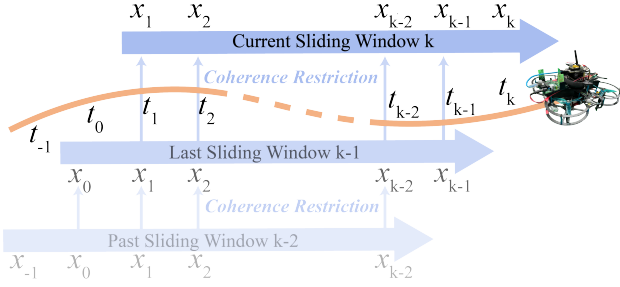


Fig. 2. Coherence restriction to exploit redundancy emerging from overlapping sliding windows.

where $\text{diag}(\mathbf{A}, \mathbf{B})$ is blockwise diagonal matrix with main diagonal blocks \mathbf{A} and \mathbf{B} .

In this way, we construct our augmented KF as follows:

$$\check{\mathbf{P}}_{f,j} = \mathbf{A}_{j-1} \hat{\mathbf{P}}_{f,j-1} \mathbf{A}_{j-1}^T + \mathbf{Q}_j \quad (12a)$$

$$\check{\mathbf{x}}_{f,j} = \mathbf{A}_{j-1} \hat{\mathbf{x}}_{f,j-1} + \mathbf{u}_j \quad (12b)$$

$$\mathbf{K}_j = \check{\mathbf{P}}_{f,j} \check{\mathbf{C}}_j^T (\check{\mathbf{C}}_j \check{\mathbf{P}}_{f,j} \check{\mathbf{C}}_j^T + \tilde{\mathbf{R}}_j)^{-1} \quad (12c)$$

$$\hat{\mathbf{P}}_{f,j} = (\mathbf{I} - \mathbf{K}_j \check{\mathbf{C}}_j) \check{\mathbf{P}}_{f,j} \quad (12d)$$

$$\hat{\mathbf{x}}_{f,j} = \check{\mathbf{x}}_{f,j} + \mathbf{K}_j (\tilde{\mathbf{y}}_j - \check{\mathbf{C}}_j \check{\mathbf{x}}_{f,j}) \quad (12e)$$

where $j = 1, 2, \dots, k_w$. And the initial step is:

$$\begin{cases} \hat{\mathbf{P}}_{f,0} = \check{\mathbf{P}}_0 \\ \hat{\mathbf{x}}_{f,0} = \check{\mathbf{x}}_0. \end{cases} \quad (13)$$

Remark 3: The label f means the \mathbf{x} and \mathbf{P} are only the intermediate temporary variables used to support the forward process, not the estimated posterior state. This means that the above results cannot be used except $\hat{\mathbf{x}}_{f,k_w}$, but we will handle this in Subsection III-C.

The augmentation in (11) can also be explained as coherence restriction, which forces the estimated state at the same timestep of nearby sliding windows to be as closer as possible. Thereby the numeric stability of calculation is enhanced.

C. Restricted Inverse-Wishart Smoother

In this subsection, we combine the backward smoother and covariance estimator together into single compact algorithm, restricted inverse-Wishart smoother. To overcome the challenge mentioned in Remark 3, we first conduct a backward smoother just the same as that in Rauch-Tung-Striebel smoother [40]:

$$\mathbf{G}_j = \hat{\mathbf{P}}_{f,j-1} \mathbf{A}_{j-1}^T \check{\mathbf{P}}_{f,j}^{-1} \quad (14a)$$

$$\hat{\mathbf{x}}_{j-1} = \hat{\mathbf{x}}_{f,j-1} + \mathbf{G}_j (\hat{\mathbf{x}}_j - \check{\mathbf{x}}_{f,j}) \quad (14b)$$

$$\hat{\mathbf{P}}_{j-1} = \hat{\mathbf{P}}_{f,j-1} + \mathbf{G}_j (\hat{\mathbf{P}}_j - \check{\mathbf{P}}_{f,j}) \mathbf{G}_j^T. \quad (14c)$$

where $j = k_w, \dots, 2, 1$, with the initial step:

$$\begin{cases} \hat{\mathbf{P}}_{k_w} = \hat{\mathbf{P}}_{f,k_w} \\ \hat{\mathbf{x}}_{k_w} = \hat{\mathbf{x}}_{f,k_w}. \end{cases} \quad (15)$$

Through this, we obtain our deserved posterior states, which are both the output of TEE and the basis for estimation of covariance matrices and aerial drag effect.

As for covariance matrices, we first assume noise covariance matrices to obey IW distribution:

$$p(\hat{\mathbf{Q}}_{k-1} | \hat{\mathbf{x}}_{0:k_w-1}) = \mathbf{IW}(\hat{\mathbf{Q}}_{k-1}; \hat{\phi}_{k-1}, \hat{\Phi}_{k-1}) \quad (16a)$$

$$p(\hat{\mathbf{R}}_{k-1} | \hat{\mathbf{x}}_{0:k_w-1}) = \mathbf{IW}(\hat{\mathbf{R}}_{k-1}; \hat{\psi}_{k-1}, \hat{\Psi}_{k-1}). \quad (16b)$$

which are known currently, since its label $k-1$ indicates it is the posterior estimation obtained by last sliding window. For the initial step, the parameters are chosen empirically and hence the PDFs are also known. The parameters of prior estimation, $\mathbf{IW}(\check{\mathbf{Q}}_k; \check{\phi}_k, \check{\Phi}_k)$ and $\mathbf{IW}(\check{\mathbf{R}}_k; \check{\psi}_k, \check{\Psi}_k)$, are calculated as follows:

$$\check{\phi}_k = w_1 (\hat{\phi}_{k-1} - n - 1) + n + 1 \quad (17a)$$

$$\check{\psi}_k = w_1 (\hat{\psi}_{k-1} - m - 1) + n + 1 \quad (17b)$$

$$\check{\Phi}_k = w_1 \hat{\Phi}_{k-1} \quad (17c)$$

$$\check{\Psi}_k = w_1 \hat{\Psi}_{k-1}. \quad (17d)$$

where $w_1 \in (0, 1]$ is a factor to reflect the weight of previous features. In the following equations of this subsection, we use $n = 6$ and $m = 4$ to represent the dimension of state and measurements respectively, for a consistent form as inverse-Wishart distribution.

Lemma 1: If the columns of the observation $\mathbf{X} = [\mathbf{x}_1, \mathbf{x}_2, \dots, \mathbf{x}_K]$ are independent and identically distributed n -dimensional Gaussian variables conforming to $\mathbf{N}(\mathbf{0}, \mathbf{C})$, with $\mathbf{C} \sim \mathbf{IW}(\sigma, \Sigma)$, then the conditional PDF has the following form:

$$p(\mathbf{C} | \mathbf{X}) = \mathbf{IW}(\mathbf{C}; \sigma + K, \Sigma + \mathbf{X}\mathbf{X}^T) \quad (18)$$

Proof: Turn to Appendix A. \square

This is the conjugation nature of inverse-Wishart distribution, and to exploit this, we formulate two auxiliary matrices:

$$\begin{aligned} \check{\Phi}_j &= \mathbb{E}[e_{1,j} e_{1,j}^T] = \hat{\mathbf{P}}_j - \mathbf{A}_{j-1} \mathbf{G}_j \hat{\mathbf{P}}_j - \mathbf{G}_j \hat{\mathbf{P}}_j \mathbf{A}_{j-1}^T \\ &\quad + \mathbf{A}_{j-1} \hat{\mathbf{P}}_{j-1} \mathbf{A}_{j-1}^T + e_{1,j} e_{1,j}^T \end{aligned} \quad (19a)$$

$$\check{\Psi}_j = \mathbb{E}[e_{2,j} e_{2,j}^T] = \mathbf{C}_j \hat{\mathbf{P}}_j \mathbf{C}_j^T + e_{2,j} e_{2,j}^T \quad (19b)$$

where the error terms are:

$$e_{1,j} = \mathbf{x}_j - \mathbf{A}_{j-1} \mathbf{x}_{j-1} - \mathbf{u}_j \quad (20a)$$

$$e_{2,j} = \mathbf{y}_j - \mathbf{C}_j \mathbf{x}_j. \quad (20b)$$

Subsequently, by applying Lemma 1, we obtain the posterior noise covariance matrices as follows:

$$\hat{\phi}_k = \check{\phi}_k + w_2 k_w \quad (21a)$$

$$\hat{\psi}_k = \check{\psi}_k + w_2 k_w \quad (21b)$$

$$\hat{\Phi}_k = \check{\Phi}_k + w_2 \sum_{j=1}^{k_w} \check{\Phi}_j \quad (21c)$$

$$\hat{\Psi}_k = \check{\Psi}_k + w_2 \sum_{j=1}^{k_w} \check{\Psi}_j \quad (21d)$$

where $w_2 \in [0, 1]$ is another factor to balance the weight of features extracted during the current sliding window.

To further suppress potential divergence led by malfunctioning sensor, we apply an additional weight to the updating

process of observation noise covariance. The sum of its auxiliary matrices is calculated in iterative form:

$$\sum_{j=1}^{k_j} \tilde{\Psi}_j = w_3 \left(\sum_{j=1}^{k_j-1} \tilde{\Psi}_j + \tilde{\Psi}_{k_j} \right) \quad (22)$$

where $k_j = 1, 2, \dots, k_w$ and $w_3 \in (0, 1)$.

Lemma 2: During the iteration of (12), if the initial state is biased as $\hat{\mathbf{x}}_{f,0} = \bar{\mathbf{x}}_0 + \delta \mathbf{x}_0$, and the final state is $\hat{\mathbf{x}}_{f,k_w} = \bar{\mathbf{x}}_{k_w} + \delta \mathbf{x}_{k_w}$, then the error propagation relation is:

$$\delta \mathbf{x}_{k_w} = \left(\prod_{j=1}^{k_w} (\mathbf{I} - \mathbf{K}_j \tilde{\mathbf{C}}_j) \mathbf{A}_{j-1} \right) \delta \mathbf{x}_0 \triangleq \mathbf{E} \delta \mathbf{x}_0 \quad (23)$$

Proof: Turn to Appendix B. \square

To find proper weights, we need to evaluate the error during the calculation process. Hence, we exploit the error propagation matrix \mathbf{E} in two ways:

$$\text{average trace: } \bar{\lambda} = \frac{1}{6} \text{tr}(\mathbf{E}) \quad (24a)$$

$$\text{reduced determinant: } \varrho = \sqrt[6]{|\mathbf{E}|} \quad (24b)$$

where $\text{tr}(\cdot)$ is the trace of square matrix (\cdot) .

For w_1 and w_2 , if $\bar{\lambda}$ is larger than a threshold $\lambda_0 \in (0, 1]$, this means the estimation is too bad to be used in covariance adjustment. And we set $w_1 = 1$ and $w_2 = 0$, so that $\hat{\mathbf{Q}}_k$ and $\hat{\mathbf{R}}_k$ remain unchanged. However, if $\bar{\lambda} < \lambda_0$, we can adjust covariance matrices, and the weights are calculated as follows:

$$w_1 = 1 - f_1 \bar{\lambda} \quad (25a)$$

$$w_2 = 1 - f_1 + f_1 \bar{\lambda} \quad (25b)$$

where $f_1 \in (0, 1)$ is a factor to control how fast the weights change. As for w_3 , we set $w_3 = f_2 + \varrho/f_2$, where $f_1 \in (0, 1)$ is another factor to control change speed. This is error propagation restriction, whose necessity and effectiveness will be thoroughly discussed in Subsection V-C.

In this way, the deserved posterior PDFs are obtained:

$$p(\hat{\mathbf{Q}}_k | \hat{\mathbf{x}}_{1:k_w}) = \mathbf{IW}(\hat{\mathbf{Q}}_k; \hat{\phi}_k, \hat{\Phi}_k) \quad (26a)$$

$$p(\hat{\mathbf{R}}_k | \hat{\mathbf{x}}_{1:k_w}) = \mathbf{IW}(\hat{\mathbf{R}}_k; \hat{\psi}_k, \hat{\Psi}_k). \quad (26b)$$

And the posterior noise covariance matrices are calculated as mathematical expectation:

$$\bar{\mathbf{Q}}_k = \mathbb{E}[\hat{\mathbf{Q}}_k] = (\hat{\phi}_k - n - 1)^{-1} \hat{\Phi}_k \quad (27a)$$

$$\bar{\mathbf{R}}_k = \mathbb{E}[\hat{\mathbf{R}}_k] = (\hat{\psi}_k - m - 1)^{-1} \hat{\Psi}_k. \quad (27b)$$

In practice, the message from the sensor may be lost or the quality of data may be poor sometimes, whereas the adaptive adjustment cannot catch up with the fast change. To handle this, a boolean amendment is included to represent the work condition of sensors:

$$\mathbf{S}_{k,i} = \begin{cases} \mathbf{I}_s, & \text{the } i\text{-th sensor functions normally} \\ \varepsilon \mathbf{I}_s, & \text{the } i\text{-th sensor malfunctions} \end{cases} \quad (28)$$

where s is the dimension of the output from the i -th sensor, and ε is a very large number. The noise covariance matrices

for practical application is finally obtained by combining (27) and (28) together:

$$\mathbf{Q}_k = \bar{\mathbf{Q}}_k \quad (29a)$$

$$\mathbf{S}_k = \text{diag}(\mathbf{S}_{k,1}, \mathbf{S}_{k,2}) \quad (29b)$$

$$\mathbf{R}_k = \mathbf{S}_k \bar{\mathbf{R}}_k \mathbf{S}_k \quad (29c)$$

where $\mathbf{S}_{k,1} \in \mathbb{R}$ and $\mathbf{S}_{k,2} \in \mathbb{R}^{3 \times 3}$ represents the work condition of UWB and optical flow sensor respectively. The algorithm of inverse-Wishart smoother in each sliding window is illustrated in Algorithm 1.

Algorithm 1: Inverse-Wishart Smoother at Time k

Input: $\tilde{\mathbf{x}}_{k-k_w:k-1}$, $\tilde{\mathbf{P}}_{k-k_w:k-1}$, $\mathbf{A}_{k-k_w:k-1}$, $\mathbf{u}_{k-k_w+1:k}$, $\mathbf{y}_{k-k_w+1:k}$, $\mathbf{C}_{k-k_w+1:k}$, $\hat{\phi}_{k-1}$, $\hat{\Phi}_{k-1}$, $\hat{\psi}_{k-1}$, $\hat{\Psi}_{k-1}$, \mathbf{E} , sensor condition

Parameter: k_w , λ_0 , f_1 , f_2 , ε

Output: $\hat{\mathbf{x}}_{0:k_w}$, $\hat{\mathbf{P}}_{0:k_w}$, $\hat{\phi}_k$, $\hat{\Phi}_k$, $\hat{\psi}_k$, $\hat{\Psi}_k$, \mathbf{Q}_k , \mathbf{R}_k

- 1 Calculate $\bar{\lambda}$ and ϱ by (24);
- 2 **if** $\bar{\lambda} \geq \lambda_0$ **then**
- 3 | $w_1 \leftarrow 1$ and $w_2 \leftarrow 0$;
- 4 **else**
- 5 | Calculate weights by (25);
- 6 **end**
- 7 Calculate prior parameters by (17);
- 8 $w_3 \leftarrow f_2 + \varrho/f_2$;
- 9 Initialize by (15);
- 10 **for** $j = k : -1 : k - k_w + 1$ **do**
- 11 | Conduct backward smoother iteration by (14);
- 12 | Calculate auxiliary matrices by (19) and (22);
- 13 **end**
- 14 Calculate posterior parameters by (21);
- 15 Calculate noise covariance matrices by (27);
- 16 Amend them with sensor condition by (28) and (29);

D. Aerial Drag Estimator

As is discussed in the introduction, aerial drag effect is essential but insufficiently researched due to complexity of UAV's aerodynamics. Thanks to the proposed sensor system, we have enough data to indirectly evaluate aerial drag effect. Under this premise, we develop a novel aerial drag estimator.

First, consider the velocity part of prior state obtained by motion model (7):

$$\tilde{\mathbf{v}}_j = (\mathbf{I}_3 - dt \cdot \boldsymbol{\mu}) \tilde{\mathbf{v}}_{j-1} + dt \cdot \mathbf{i}_k \quad (30)$$

where $\tilde{\mathbf{v}}_j$ and $\hat{\mathbf{v}}_{j-1}$ are velocity part of $\tilde{\mathbf{x}}_j$ and $\hat{\mathbf{x}}_{j-1}$ respectively. Also, with measurements from sensor system, we obtain $\hat{\mathbf{x}}_j$. Our goal is to adjust $\boldsymbol{\mu}$ such that $\tilde{\mathbf{x}}_j$ approaches $\hat{\mathbf{x}}_j$, and hence we can formulate a cost function:

$$J_j = \|\tilde{\mathbf{v}}_j - \hat{\mathbf{v}}_j\|_2^2 = (\tilde{\mathbf{v}}_j - \hat{\mathbf{v}}_j)^T (\tilde{\mathbf{v}}_j - \hat{\mathbf{v}}_j) \quad (31)$$

which is a quadratic form w.r.t. $\boldsymbol{\mu}$. By taking the derivative:

$$\frac{\partial J_j}{\partial \boldsymbol{\mu}} \Big|_{\tilde{\mathbf{v}}_{j-1}, \hat{\mathbf{v}}_j} = 2dt (\tilde{\mathbf{v}}_j - (\mathbf{I}_3 - dt \boldsymbol{\mu}) \tilde{\mathbf{v}}_{j-1} - \hat{\mathbf{v}}_j)^T \hat{\mathbf{v}}_{j-1}^T, \quad (32)$$

we can conduct a gradient descent method to amend μ :

$$\mu \leftarrow \mu - \ell_k \cdot \frac{\partial J_j}{\partial \mu} \Big|_{\hat{v}_{j-1}, \hat{v}_j} \quad (33)$$

where ℓ_k is step length.

Remark 4: Although we can find the global minimum of a quadratic cost function easily, we still choose the gradient descent method instead of calculating the extremum point directly. In this way, we can maintain the numeric stability and prevent the updating step from fierce oscillation.

Since the choice of proper step length is a critical issue in gradient descent, we advisedly design a strategy to accomplish this. The noise covariance matrices inherently reflect the deviation of motion and observation models respectively, w.r.t. true situation, and hence they are natural indicators to evaluate the performance of both models. Under this premise, we calculate ℓ_k as follows:

$$\ell = \begin{cases} 0, & \sqrt[6]{|\mathbf{Q}_k|} \leq \sqrt[4]{|\mathbf{R}_k|} \\ b_u - \frac{(b_u - b_l) \sqrt[4]{|\mathbf{R}_k|}}{\sqrt[6]{|\mathbf{Q}_k|}}, & \sqrt[6]{|\mathbf{Q}_k|} > \sqrt[4]{|\mathbf{R}_k|} \end{cases} \quad (34)$$

where b_u and b_l are upper and lower bounds for step length.

Intuitively, if $\sqrt[6]{|\mathbf{Q}_k|} \leq \sqrt[4]{|\mathbf{R}_k|}$, the sensors are less reliable than the motion model, and hence we shouldn't amend μ with measurements. On the other hand, once $\sqrt[6]{|\mathbf{Q}_k|} > \sqrt[4]{|\mathbf{R}_k|}$, we can start our adjustment. And as $\sqrt[4]{|\mathbf{R}_k|}$ gets smaller, ℓ grows from its lower bound to upper bound.

E. Ternary Evolving Estimator

As is shown in Fig. 1, every part is tightly connected with each other, and hence we compress them into one compact algorithm, ternary evolving estimator (TEE). In our work, we delve into the inner connection of each part and construct several restrictions. Firstly, augmented Kalman filter processes all data from sensor system and last sliding window under coherence restriction. Additionally, to maintain numerical stability, we apply consistency restriction which keeps all parameters in one sliding window to be the same. Then processed data are sent to backward smoother yielding posterior states as output. Subsequently, the posterior states are utilized to estimate noise covariance matrices under error propagation restriction and sensor condition restriction. Notably, the backward smoother and covariance estimation are joint together into restricted inverse-Wishart smoother in Algorithm 1. After that, the covariance matrices together with posterior states are employed to adjust aerial drag matrix via gradient descent. In return, all obtained data are prepared for next sliding window to conduct augmented Kalman filter filter. In this way, TEE is highly adaptive to the change of surroundings, strongly robust to the interference from harsh environments, and rapidly recovers from the disturbance in a resilient way. The full algorithm of TEE is exhibited in Algorithm 2.

IV. ANALYSIS

A. Observability of Sensor System

The observability matrix of sensor system modeled by (7) and (10) is:

$$\mathbf{O}_k = [\mathbf{C}_k^T \quad \mathbf{A}_{k-1}^T \mathbf{C}_k^T \quad \cdots \quad \mathbf{A}_{k-1}^{5T} \mathbf{C}_k^T]^T \quad (35)$$

Algorithm 2: Ternary Evolving Estimator at Time k

Input: $\tilde{\mathbf{x}}_{k-k_w:k-1}$, $\tilde{\mathbf{P}}_{k-k_w:k-1}$, $\boldsymbol{\mu}$, dt , $\mathbf{u}_{k-k_w+1:k}$, $\mathbf{y}_{k-k_w+1:k}$, $\hat{\phi}_{k-1}$, $\hat{\Phi}_{k-1}$, $\hat{\psi}_{k-1}$, $\hat{\Psi}_{k-1}$, and sensor condition

Parameter: k_w , λ_0 , f_1 , f_2 , ε , b_l , b_u

Output: $\hat{\mathbf{x}}_{k-k_w:k}$, $\hat{\phi}_k$, $\hat{\Phi}_k$, $\hat{\psi}_k$, $\hat{\Psi}_k$, $\boldsymbol{\mu}$

- 1 Calculate \mathbf{Q} and \mathbf{R} by (27);
- 2 Amend them with sensor condition by (28) and (29);
- 3 Calculate $\mathbf{A}_{k-k_w:k-1}$ by (7);
- 4 Calculate $\mathbf{C}_{k-k_w+1:k}$ by (9) and (10);
- 5 Augment $\mathbf{y}_{k-k_w+1:k}$, $\mathbf{C}_{k-k_w+1:k}$ and \mathbf{R} by (11);
- 6 Initialize by (13);
- 7 **for** $j = k - k_w + 1 : +1 : k$ **do**
- 8 | Conduct Kalman filter by (12);
- 9 **end**
- 10 Calculate \mathbf{E} by (23);
- 11 Run Algorithm 1;
- 12 Calculate step length by (34);
- 13 **for** $j = k - k_w + 1 : +1 : k$ **do**
- 14 | Calculate derivative by (32);
- 15 | Update $\boldsymbol{\mu}$ by (33);
- 16 **end**

where $\mathbf{A}^{nT} = (\mathbf{A}^n)^T = (\mathbf{A}^T)^n$ for brevity.

Theorem 1: If $\mathbf{p}_k \neq \mathbf{0}$ and $\text{dt} \cdot \boldsymbol{\mu} \neq \mathbf{I}$, then $\text{rank}(\mathbf{O}_k) = 6$ and this system is observable.

Proof: We select a submatrix of \mathbf{O} that has the form:

$$\tilde{\mathbf{O}} = \frac{\mathbf{I}_6 \otimes \tilde{\mathbf{p}}^T}{\|\tilde{\mathbf{p}}\|_2} \begin{bmatrix} \mathbf{I}_3 & \text{dt} \cdot \mathbf{X}_0 \\ \vdots & \vdots \\ \mathbf{I}_3 & \text{dt} \cdot \mathbf{X}_5 \end{bmatrix} \in \mathbb{R}^{6 \times 6} \quad (36)$$

where the label k is omitted. And $\mathbf{X}_{i+1} = \mathbf{I}_3 + \mathbf{X}_i(\mathbf{I}_3 - \text{dt}\boldsymbol{\mu})$ with $\mathbf{X}_0 = \mathbf{0}_3$. The details of \mathbf{X} 's are shown in Appendix C. It shows that every row of $\tilde{\mathbf{O}}$ is independent of one another, which means $\text{rank}(\tilde{\mathbf{O}}) = 6$. Also, $\text{rank}(\tilde{\mathbf{O}}) \leq \text{rank}(\mathbf{O}_k) \leq 6$ because of submatrix's property. Hence, $\text{rank}(\mathbf{O}_k) = 6$. \square

The conditions of Theorem 1 make sense. If $\mathbf{p}_k \approx \mathbf{0}$, this means the UAV is almost at the same position as UWB, and hence UWB fails. But in practical application, UAV hardly hovers near the anchor but usually flies far away instead. On the other hand, in common aerial surroundings, drag effect is very small and $\text{dt} \cdot \boldsymbol{\mu} \ll \mathbf{I}$. Furthermore, even if one of the conditions fails, this won't last long and the sliding window can handle this by evaluating a long trajectory which is observable almost everywhere.

Theorem 2: The observability of augmented model in (11) is guaranteed without any additional condition.

Proof: The proof is almost the same as Theorem 1. Since \mathbf{C}_k is augmented with an identity matrix, we can directly select a submatrix \mathbf{I}_6 from the observability matrix. Hence, the augmented model is observable. \square

However, at timestep k_w , there is no augmentation, and the observability relies on Theorem 1. But as is mentioned before, we exploit the advantage of sliding window to overcome the potential problem.

B. Convergence of State Estimation

This subsection is focused on the pre-processing filter and backward state channel of TEE shown in Fig. 1.

Theorem 3: The combination of forward process by (12) and backward process by (14) is equivalent to a maximum a posteriori (MAP) process with the analytic solution:

$$\hat{\mathbf{x}}_{0:k_w} = (\mathbf{H}^T \mathbf{W}^{-1} \mathbf{H})^{-1} \mathbf{H}^T \mathbf{W}^{-1} \mathbf{z} \quad (37)$$

and auxiliary matrices:

$$\mathbf{z} = [\hat{\mathbf{x}}_{0:k_w-1}^T, \mathbf{v}_{1:k_w}^T, \mathbf{y}_{1:k_w}^T]^T \quad (38a)$$

$$\mathbf{H} = \begin{bmatrix} [\mathbf{I}_{6k_w}, \mathbf{0}_{6k_w \times 6}] \\ \tilde{\mathbf{I}}_A \\ [\mathbf{0}_{4k_w \times 6}, \text{diag}(\mathbf{C}_{1:k_w})] \end{bmatrix} \quad (38b)$$

$$\mathbf{W} = \text{diag}(\tilde{\mathbf{P}}_{0:k_w-1}, \mathbf{Q}_{1:k_w}, \mathbf{R}_{1:k_w}) \quad (38c)$$

where $\text{diag}(\mathbf{C}_{i:j})$ denotes blockwise diagonal matrix with main diagonal blocks $\mathbf{C}_i, \mathbf{C}_{i+1}, \dots, \mathbf{C}_j$ and

$$\tilde{\mathbf{I}}_A = \begin{bmatrix} -\mathbf{A}_0 & \mathbf{I} & & & & \\ & & \ddots & & & \\ & & & \ddots & & \\ & & & & -\mathbf{A}_{k_w-1} & \mathbf{I} \end{bmatrix}. \quad (39)$$

Proof: We recommend reader to refer to Chapter 3 in [23]. It reformulates original MAP and derives the famous Rauch-Tung-Striebel smoother (RTSS) after tons of mathematical manipulation. In this way, the conditions and solution space remain unchanged, Also, with augmentation in (11), the our estimator is consistent with RTSS in format. Hence, the equivalence is true. \square

Since MAP yields theoretically optimal estimation, it guarantees the convergence of our proposed method. This also means the effectiveness of estimation is right at the Cramér-Rao Lower Bound.

From the perspective of MAP, we can also construct the logarithm likelihood function for it:

$$\ln L(\mathbf{x}_{0:k_w}) = \sum_{i=1}^{k_w} J_{1,i} + \sum_{j=1}^{k_w} J_{2,j} + \sum_{k=0}^{k_w-1} J_{3,k} \quad (40)$$

where $\ln(\cdot)$ is the natural logarithm of scalar (\cdot) . The function J_1 's and J_2 's are responsible for the motion and observation models respectively, and J_3 's represent the inherent restriction we introduced before:

$$J_{1,i} = \mathbf{e}_{1,i}^T \mathbf{Q}_i^{-1} \mathbf{e}_{1,i} \quad (41a)$$

$$J_{2,i} = \mathbf{e}_{2,i}^T \mathbf{R}_i^{-1} \mathbf{e}_{2,i} \quad (41b)$$

$$J_{3,i} = (\mathbf{x}_i - \tilde{\mathbf{x}}_i)^T \tilde{\mathbf{P}}_i^{-1} (\mathbf{x}_i - \tilde{\mathbf{x}}_i). \quad (41c)$$

where $\mathbf{e}_{1,i}$ and $\mathbf{e}_{2,i}$ are error terms in (20).

Based on this premise, we have a better understanding of (11). The additional cost functions J_3 's exert a coherence restriction, which forces the estimation to be smoother through the trajectory. Also, the covariance matrices are weights of cost functions, which counts for our effort to estimate covariance, and helps to leverage all data.

C. Sensitivity of Covariance Estimation

For the covariance estimator of TEE, the weights introduced in (17), (21) and (22) do have some degree of influence on solving process. Also, the initially and empirically chosen PDFs mentioned after (16) will affect the estimation. In this subsection, we will analyse their effects. To guarantee generality of the analysis, in this subsection, we use n and m to represent the dimension of state and measurements respectively. And in our work, we have $n = 6$ and $m = 4$.

Theorem 4: Given initial knowledge $\mathbf{Q}_0 = (\hat{\phi}_0 - n - 1)^{-1} \hat{\Phi}_0$, and denoting $\hat{\phi}_k - n - 1 \triangleq \zeta(k)$, we have:

$$\mathbf{Q}_k = \left(\prod_{i=1}^k \eta(i) \right) \mathbf{Q}_0 + \sum_{i=1}^k \left(\prod_{j=i+1}^k \eta(j) \right) \boldsymbol{\xi}(i) \quad (42)$$

where for succinct expression we define:

$$\eta(k) = \frac{\zeta(k)}{\zeta(k) + w_2 k_w} \quad \text{and} \quad \boldsymbol{\xi}(k) = \frac{\sum_{r=1}^{k_w} \tilde{\Phi}_r}{\zeta(k) + w_2 k_w}. \quad (43)$$

Proof: Substituting (17), (19) and (21) into (27) yields:

$$\mathbf{Q}_k = \frac{w_1 \hat{\Phi}_{k-1} + w_2 \sum_{r=1}^{k_w} \tilde{\Phi}_r}{w_1 (\hat{\phi}_{k-1} - n - 1) + w_2 k_w}. \quad (44)$$

Meanwhile, according to (27) we have $\mathbf{Q}_{k-1} = (\hat{\phi}_{k-1} - n - 1)^{-1} \hat{\Phi}_{k-1}$. Compare the two equations yielding:

$$\mathbf{Q}_k = \eta(k) \mathbf{Q}_{k-1} + \boldsymbol{\xi}(k) \quad (45)$$

which can be reformed into a geometric series:

$$\mathbf{Q}_k + \frac{\boldsymbol{\xi}(k)}{\eta(k) - 1} = \eta(k) \left(\mathbf{Q}_{k-1} + \frac{\boldsymbol{\xi}(k)}{\eta(k) - 1} \right). \quad (46)$$

Hence we can easily obtain (42). \square

Theorem 5: Given initial knowledge $\bar{\mathbf{R}}_0 = (\hat{\psi}_0 - n - 1)^{-1} \hat{\Psi}_0$, we have:

$$\mathbf{S}_k^{-1} \mathbf{R}_k \mathbf{S}_k^{-1} = \left(\prod_{i=1}^k \tilde{\eta}(i) \right) \bar{\mathbf{R}}_0 + \sum_{i=1}^k \left(\prod_{j=i+1}^k \tilde{\eta}(j) \right) \tilde{\boldsymbol{\xi}}(i) \quad (47)$$

where the superscript tilde means the $\hat{\phi}$'s and $\tilde{\Phi}$'s in them are replaced by $\hat{\psi}$'s and $\tilde{\Psi}$'s correspondingly.

Proof: It is parameters $\hat{\psi}$ and $\hat{\Psi}$ that propagate throughout the process. Only when we want to get \mathbf{R}_k , is \mathbf{S}_k employed in calculation. The slight difference in calculating sum of auxiliary matrices via (22) also doesn't affect the proof. Hence the proof is the same as Theorem 4. \square

Lemma 3: Given initial knowledge $\mathbf{Q}_0 = (\hat{\phi}_0 - n - 1)^{-1} \hat{\Phi}_0$, we have the degree of freedom parameter at timestep k as:

$$\hat{\phi}_k = w_1^k (\hat{\phi}_0 - n - 1) + n + 1 + w_2 k_w (w_1 - w_1^k) / (1 - w_1). \quad (48)$$

Proof: Combining (17) and (21) yields:

$$\hat{\phi}_k = w_1 (\hat{\phi}_{k-1} - n - 1) + n + 1 + w_2 k_w \quad (49)$$

which can be reformed into:

$$\hat{\phi}_k - n - 1 + \frac{w_2 k_w}{w_1 - 1} = w_1 (\hat{\phi}_{k-1} - n - 1 + \frac{w_2 k_w}{w_1 - 1}). \quad (50)$$

This is a geometric series and we can easily obtain (48). \square

Since \mathbf{Q}_k and \mathbf{R}_k obey the same distribution and has symmetric form, we can obtain the same conclusion for $\hat{\psi}_k$ as

$\hat{\phi}_k$ in Lemma 3, just by replacing corresponding parameters. Hence, according to Theorem 4 and Theorem 5, by applying Lemma 3 to replace $\hat{\phi}_k$ and $\hat{\psi}_k$, we see that:

$$\lim_{k \rightarrow +\infty} \eta(k) \text{ or } \tilde{\eta}(k) = w_1 \in (0, 1]. \quad (51)$$

This means as time passes by the effect of previous features declines while the currently extracted features count more. And no matter what initial PDFs or weights are chosen, the information inherited from the initial PDFs has nothing left, and only the recent knowledge counts. Also, the initial covariance matrices are positive-definite and all ξ 's or $\tilde{\xi}$'s are guaranteed by (19) to be positive-definite as well. We know that the linear combination of positive-definite matrices remains positive-definite. As for the choice of weights by (25), it just control the speed of forgetting previous information, but the value of weights is always within the convergence field. Hence, the convergence of covariance estimation is low-sensitive to initial parameter selection.

D. Arithmetic Complexity of Algorithm

The state dimension, measurement dimension and size of sliding window are denoted by n , m and k respectively. We assume four arithmetic operations, comparison and evaluation all take the same time units.

Theorem 6: The arithmetic complexity of Algorithm 2 is $\mathcal{O}(k(n^3 + n^2m + nm^2 + m^3))$.

Proof: The augmented Kalman filter is of the greatest complexity $\mathcal{O}(k(n^3 + n^2m + nm^2 + m^3))$. And inverse-Wishart smoother in Algorithm 1 is of $\mathcal{O}(k(n^3 + n^2m + m^2))$, while aerial drag estimator is of $\mathcal{O}(kn^2)$. All other lines are not iterated in sliding window and can be omitted. \square

In practice, the dimension of state and measurements are quite smaller than size of sliding window. Theorem 6 shows the linear complexity w.r.t. k , which suggests the efficiency of proposed method. As for traditional method, MAP in (37), its arithmetic complexity is $\mathcal{O}(k^3n(n^2 + nm + m^2))$, which is cubic. And the state-of-the-arts in [37], is of quadratic complexity $\mathcal{O}(k^2tn(n^2 + nm + m^2) + kt^2n^2(m + n) + t^3n^3)$ by employing polynomial approximation, where t is degree of polynomial and much smaller than k . Thanks to efficiency of augmented Kalman filter, we can spare more computational resource for adaptive evolution of parameters.

V. EXPERIMENTS

A. Experimental Setup

In all experiments, a VICON[®] motion capture system is employed to record ground truth with a frequency of 200Hz. The quadrotor unmanned aerial vehicle is steered under the control of the open-source Pixhawk[®]. An NVIDIA[®] NX computing mounted Intel Atom x7 (four cores, 1.8 GHz) is employed as the onboard computer. The IMU, module CHCNAV CL-510, is utilized for acceleration measurements. The Nooploop[®] UWB (model LinkTrack LTPS[®]) is selected for range measurement cooperated with a fixed anchor also equipped with the same UWB. The optical flow, module NiMing v4, is adopted for velocity measurements. Since

this section is mainly focused on the performance of state estimation, the design of controller is simplified. The UAV is controlled manually or by a simple proportional-integral-differential algorithm to fly along a circular trajectory, and the IMU, UWB, and optical flow measurements are collected at a frequency of 25Hz.

We conduct experiments with different velocity in common laboratory surroundings and record three datasets, namely B_1 to B_3 . To evaluate our method in harsh environments, we repeat experiments also with different velocity with blinking light and a smoke generator, and record four datasets Y_0 to Y_3 . To overcome jagged edges in data due to simplified controller and poor physical structure lacking vibration damping, we apply a Savitzky–Golay filter with polynomial order 3 and frame length 9 to estimated position. The configuration of the aforementioned testbed is illustrated in Fig. 3. And the parameters in experiments are displayed in Appendix D.

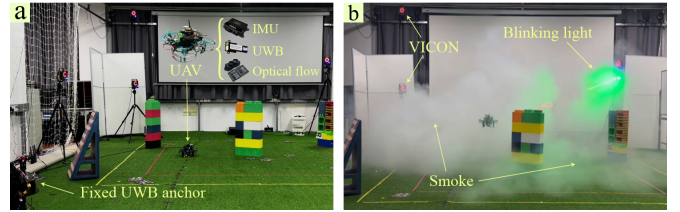


Fig. 3. Testbeds of experiments. Subfigure (a) shows common surroundings; subfigure (b) is smoky and blinking environment.

B. Evaluation of Overall Performance

To assess effectiveness and stability of proposed method, we compare it to the state-of-the-art, DWE in [37], which has the same form as (37)–(39), but cannot adjust its parameters. The results are displayed in Table I, where we evaluate the root mean square error (RMSE) and the standard deviation (STD) of three axes.

TABLE I
OVERALL PERFORMANCE COMPARISON BETWEEN DWE AND TEE

Data Set	Method	RMSE(m)			STD(m)		
		x	y	z	x	y	z
B_1	DWE	0.07	0.14	0.05	0.04	0.07	0.03
	TEE	0.07	0.14	0.03	0.04	0.09	0.02
B_2	DWE	0.08	0.13	0.06	0.05	0.08	0.02
	TEE	0.09	0.11	0.05	0.06	0.07	0.02
B_3	DWE	0.24	0.38	0.11	0.15	0.19	0.06
	TEE	0.14	0.11	0.05	0.10	0.07	0.03
Y_0	DWE	0.32	0.62	0.09	0.20	0.38	0.05
	TEE	0.25	0.25	0.05	0.15	0.17	0.03
Y_1	DWE	0.19	0.43	0.06	0.11	0.26	0.03
	TEE	0.23	0.22	0.08	0.13	0.14	0.06
Y_2	DWE	0.17	0.35	0.10	0.10	0.26	0.08
	TEE	0.22	0.19	0.15	0.11	0.13	0.12
Y_3	DWE	0.39	0.43	0.24	0.23	0.27	0.22
	TEE	0.37	0.38	0.06	0.25	0.25	0.04

From the results, it proves the proposed method TEE significantly outperforms DWE, especially in harsh environments,

Y_0 to Y_3 . In common environments, however, TEE may not always show its advantage since the noise covariance matrices and aerial drag matrix seldom change much. The typical estimation results of dataset B_2 is illustrated in Fig. 4. Notably, TEE reduces the error along x-axis and y-axis to the same degree, whereas DWE always leaves one axis worse. This is because noise covariance matrices are natural weights, and TEE adjusts them accordingly to balance the error. But without adaptive adjustment, the weights of two axes are empirically set to be the same, which conflicts with the fact and causes performance degradation of DWE.

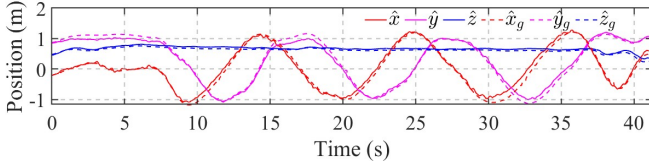


Fig. 4. Typical position estimation results of TEE on dataset B_2 , where dotted line and label "g" are used to denote ground truth from VICON.

As illustrated in subfigure (a) of Fig. 5, for the typical experiment B_2 , the diagonal entry of process noise covariance matrix corresponding to y-axis is larger than that corresponding to x-axis, which is consistent with DWE result that RMSE along y-axis is larger than that along x-axis. Although the symmetry of aerodynamics indicates the weights corresponding to x-axis and y-axis should be the same, the measurements from UWB causes this difference. It only provides distance information, which is a weak constraint of only one dimension. The limited dimension of information leads to the fact that in practice estimation along one axis usually performs worse than the other. On the other hand, it is optical flow sensor that plays a part in velocity estimation, while UWB doesn't affect this process. Hence we see $Q_{44} = Q_{55}$, which agrees with the symmetry of aerodynamics. Thanks to our algorithm, the process noise covariance matrix becomes competent to reveal these points, which helps estimator to find better weights.

For observation noise covariance matrix in subfigure (b), we evaluate its shape parameter here instead of covariance matrix itself since its change is slight and uneasy for intuitive understanding ought to error propagation restriction (22). It shows that entry corresponding to UWB is the largest one, because this range odometry is always not sufficiently accurate and can only provide a global reference. As for optical flow sensor, entries of x-axis and y-axis are the same due to symmetry and entry of z-axis is slightly larger than them since vertical velocity obtained by difference method is less precise than horizontal velocity obtained by optical flow method. In this way, TEE makes full use of information from sensors and tries its best to avoid divergence led by malfunctioning sensor.

C. Validation of Inherent Restrictions

As is mentioned before, we apply several inherent restrictions to overcome sensor malfunction and suppress potential divergence. In this subsection, we delve into the effects of them. Here we evaluate three axes together using RMSE of Euclidean distance between estimated position and ground

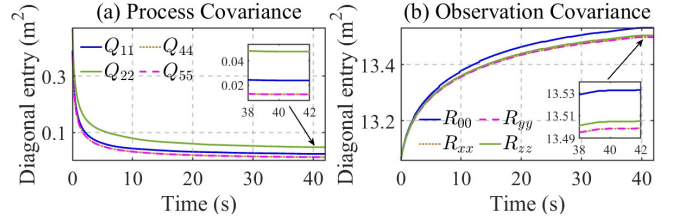


Fig. 5. Diagonal entry changing tendency of noise covariance matrices (dataset: B_2). Subfigure (a) shows entries of process noise covariance matrices where Q_{11} , Q_{22} , Q_{44} and Q_{55} are corresponding to x-position, y-position, x-velocity and y-velocity respectively; subfigure (b) shows entries of observation noise covariance matrices where R_{00} is corresponding to UWB while the others are corresponding to three axes of optical flow sensor.

truth, $\sqrt{\frac{1}{n} \sum_{i=1}^n \|\mathbf{p}_i - \mathbf{p}_{i,g}\|_2^2}$, instead of examining three separated axes. All results are displayed in Table II, where "none" denotes original TEE the same as that in Table I.

TABLE II
RMSE COMPARISON BETWEEN MODIFIED TEEs WITH CERTAIN RESTRICTION CANCELLED (UNIT: M)

Cancelled Restriction	B_1	B_2	B_3	Y_0	Y_1	Y_2	Y_3
None	0.16	0.15	0.19	0.35	0.33	0.33	0.54
ErrProp	0.16	0.15	0.20	0.45	0.45	0.43	0.59
coherence	1.27	1.04	1.49	1.50	1.44	1.55	1.78
Consist	0.94	1.04	4.04	1.57	2.28	1.23	1.83

Among all restrictions, the most complicated one is error propagation restriction (abbr. ErrProp or EP), (23)–(25). We cancel this restriction by setting three weights in (17), (21) and (22) to be 1, $w_1 = w_2 = w_3 = 1$. From the results, we see in common environments, whether cancel it or not doesn't affect estimation precision much. In harsh environments, however, the estimation deteriorates after the restriction is canceled. This shows TEE's advantage in handling harsh environments, as shown in Fig. 6. Without error propagation restriction, the estimator can hardly track the position especially when UAV takes a sharp turn, because it has been used to mild movement, which serves as a foil to the high adaptability of TEE.

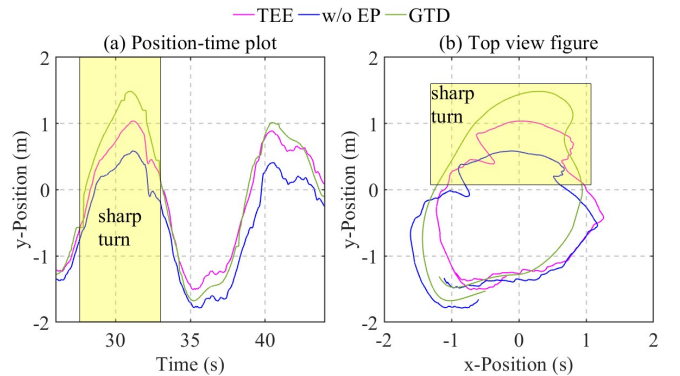


Fig. 6. Comparison between estimations with and without error propagation restriction on sharp turn of dataset Y_2 , where "GTD" means ground truth from VICON.

Another perspective is illustrated in Fig. 7. The estimation is interfered by sudden rapid fluctuations at first, and TEE

gradually recovers from divergence, whereas the one without restriction is misled by malfunctioning sensor leaving an estimation bias. The root cause of position estimation divergence in subfigure (a) is the divergence of velocity estimation shown in subfigure (b). The height laser of optical flow sensor (abbr. OF) mistakes smoke particles as ground and measures wrong z-velocity, which misleads velocity estimation. Thanks to error propagation restriction, velocity estimation converges again soon, which results in gradual convergence of position estimation through integral relation.

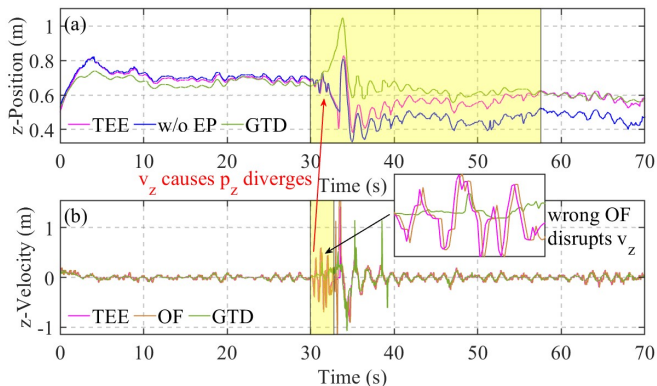


Fig. 7. Position and velocity estimation of TEE on dataset Y_1 with sudden rapid fluctuations, where “GTD” means ground truth from VICON. Subfigure (a) is comparison along z-axis between TEE and that without error propagation restriction; subfigure (b) shows the reason of divergence and recovery.

Aerial drag estimation is also affected at the beginning of sudden fluctuations, since the calculation of its gradient (32) relies directly on velocity estimation. The changing tendency of aerial drag estimation on dataset Y_1 is illustrated in subfigure (a) of Fig. 8. A sharp increasing curve emerges at first due to fluctuations, but soon later it is replaced by a horizontal line. This is because those wrong adaptive adjustments are stopped by error propagation restriction, and subfigure (b) shows how parameters respond to fluctuations. Soon after rapid fluctuations, adjustments continues and converges again. Notably, the details of convergent line shows that it has slight oscillation at the micro scale even if it seems horizontal in subfigure (a), which is different from the horizontal line resulted from error propagation restriction.

The error propagation matrix acutely perceives anomalous estimation. As is shown in subfigure (b) of Fig. 8, the diagonal entry corresponding to z-velocity, E_{66} , responds to sudden fluctuations but the entry corresponding to z-position, E_{33} , remains almost unchanged. That is because position estimation is based on velocity estimation via integral, and the calculation process itself is normal although the results are misled. This shows the proficiency of \mathbf{E} in (23) to serve as an online inspector of error. The parameters in (24) are also displayed in subfigure (b), where the average trace (abbr. AveTrc) is more sensitive to slight interference, and the reduced determinant (abbr. RedDet) focuses on significant fluctuations more. This proves effective to merge these two parameters in error propagation restriction.

The second restriction is coherence restriction, which is employed to exploit redundant information due to overlapping

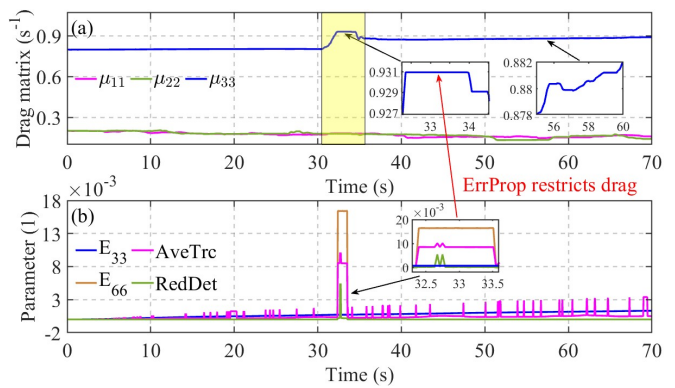


Fig. 8. Error propagation restriction prevents aerial drag estimation from divergence. Subfigure (a) illustrates diagonal entry changing tendency of aerial drag matrix. Subfigure (b) displays changing tendency of parameters in (24) and diagonal entry of error propagation matrix in (23).

sliding windows, as illustrated in Fig. 2. We remove it by simply omitting the augmentation step for KF (11). This makes the observability no longer guaranteed by Theorem 2 and reduced to a weaker one in Theorem 1. What’s more, our estimator highly relies on coherence restriction to inherit historical information, since the size of sliding window is 10 in our experiments, which is typically too small to perform proper estimation. Hence, as is shown in Table I, every estimation has significant error with coherence restriction cancelled.

To keep numerical stability, we apply one additional restriction called consistency restriction. When TEE begins in every new sliding window, we re-initialize $\hat{\mathbf{P}}_0 = 0.1 \cdot \mathbf{I}_6$, and we keep all \mathbf{Q} ’s and \mathbf{R} ’s the same for every timestep, which are obtained by Algorithm 1 in last sliding window. To cancel this restriction, we use a matrix sequence of size $k_w + 1$ to record historical covariance matrices \mathbf{P} ’s, \mathbf{Q} ’s and \mathbf{R} ’s. In this way, all the noise covariance matrices at each timestep differ from one another. And hence the estimator becomes more numerically sensitive, which increase probability of divergence. This counts for the results that diverges badly. On the other hand, since the size of sliding window is quite small, it is rational to assume all covariance matrices are approximately the same.

As is illustrated in Fig. 9, we consider the ratio between reduced determinant of noise covariance matrices to evaluate the performance of four methods in Table II. The calculation of reduced determinant is the same as that in (24), which is the geometric mean of eigenvalues and reflects the overall tendency of the matrix. The ratio of original TEE grows steadily, but the slope is getting smaller and smaller, which indicates its stability. The growing ratio means the estimator has more and more confidence in observation model, and it trusts the adjusted covariance matrices more as time goes by, which creates a virtuous circle. With error propagation restriction cancelled, the estimator is more sensitive to surrounding interference. The sudden fluctuations has strong impact on the ratio and hence the estimation is misled to bias. Without consistency restriction, the estimator is even more sensitive, to not only interference, but small numerical changes also. Its amplitude of ratio oscillation is hundred times greater than

other three ones, which counts for its divergence. As for the one without coherence restriction, since the performance is too bad, the error propagation restriction forces estimator to stop all adaptive adjustments. As a result, the ratio remains unchanged. The conclusion is that coherence and consistency restrictions are fundamental to our estimator, while error propagation restriction is essential to handle harsh environments, which is a significant difference to distinguish our method from other adaptive filters.

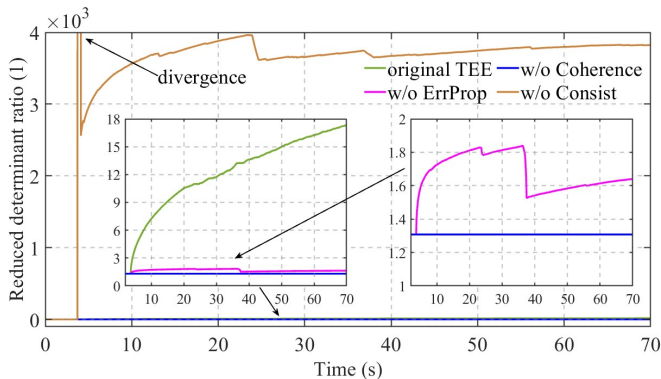


Fig. 9. Changing tendency of reduced determinant ratios, $\sqrt[6]{|Q|}/\sqrt[4]{|R|}$, of noise covariance matrices on dataset Y_1 .

D. Verification of Aerial Drag Estimation

Aerial drag effect has proven essential for UAV positioning, and in our work, we innovatively design a method to estimate aerial drag matrix. In this subsection, we verify the effectiveness and necessity of aerial drag adjustment. We consider two situations to compare performance between TEE and that without drag adjustment. The results are displayed in Table III, where the first row is standard TEE with the same μ_0 as that in Appendix D.

TABLE III
RMSE COMPARISON BETWEEN MODIFIED TEEs WITH DIFFERENT AERIAL DRAG SETTINGS (UNIT: M)

Initial Drag	Adjust Or Not	B_1	B_2	B_3	Y_0	Y_1	Y_2	Y_3
μ_0	yes	0.16	0.15	0.19	0.35	0.33	0.33	0.54
0_3	yes	0.16	0.17	0.19	0.37	0.33	0.40	0.58
	no	0.16	0.15	0.18	0.36	0.33	0.38	0.57
$25I_3$	yes	0.26	0.24	0.22	0.65	0.54	0.66	0.81
	no	0.56	0.46	0.51	0.66	0.64	0.69	0.91

First, we assume no drag by setting initial aerial drag matrix to be zero. We see the RMSE of both methods doesn't show significant difference, since gradient calculated by (32) is related to last aerial drag matrix μ , which means the result of adjustment is still close to zero. Sometimes, the performance of TEE with drag adjustment is slightly worse than that without drag adjustment. This is because interference plays a more important role when μ is quite small. Hence the gradient is more numerically sensitive, which means aerial drag estimation is more likely to be trapped in oscillation,

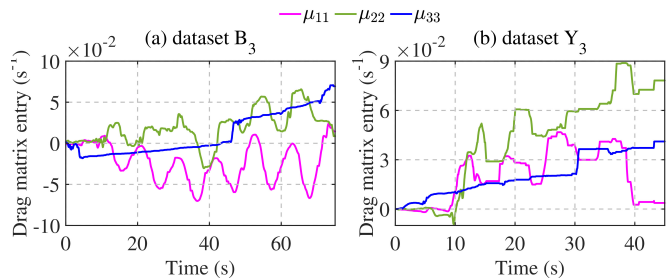


Fig. 10. Oscillation in diagonal entry of aerial drag matrix with zero initial drag. Subfigures (a) and (b), sharing the same axis labels, are tested on dataset B_3 and Y_3 respectively.

as is illustrated in Fig. 10. With zero initial drag, however, performance generally shows no better than original TEE in Table II, whether adjust or not, and especially bears a precision loss in harsh environments. This indicates the necessity of taking aerial drag effect into account, which is critical to both preventing aerial drag estimation from oscillation and achieving better positioning performance.

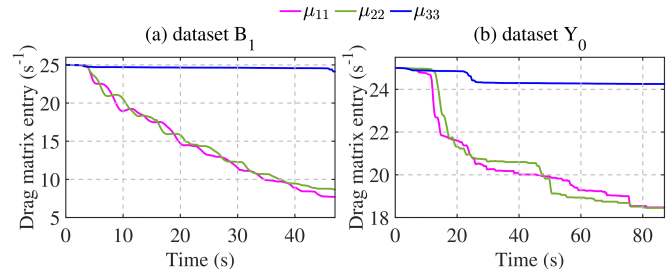


Fig. 11. Diagonal entry changing tendency of aerial drag matrix with wrong initial drag. Subfigures (a) and (b), sharing the same axis labels, are tested on dataset B_1 and Y_0 respectively.

Secondly, we test the adaptability of proposed method when we set wrong initial drag. As is discussed in Theorem 1, we need $dt \cdot \mu \neq I$ to keep observability. Hence we intentionally choose $\mu_0 = I_3/dt$ here. From Table III, it shows TEE with drag adjustment significantly outperforms that without drag adjustment in all datasets. Unlike zero initial drag, this wrong drag is big enough for gradient calculation, so that it's not quite sensitive to interference and can find relatively proper value. The performances of aerial drag adjustment of dataset B_1 and Y_0 are illustrated in Fig. 11. The diagonal entry corresponding to z-axis doesn't change much, because UAV flies along a horizontal circle and z-velocity is approximately zero almost all the time. The entries corresponding to x-axis and y-axis decrease gradually as time goes by, which makes estimation more and more accurate. However, one weakness is that gradient descent method cannot guarantee a global optimum, since the problem is not convex enough. But if we choose an empirically proper initial value, it always converges to a local optimum, which proves sufficiently effective in practical application.

E. Comparison of Different Adjustment Frequency

In this section, we discuss the effectiveness of adaptive adjustment from another interesting perspective. We compare

impact of different adjustment frequency on estimation performance. The results are displayed in Table IV, where we use ratio of adjustment period to estimation period as an indicator. The ratio "1" and "N/A" denotes original TEE and DWE respectively, which are the same as those in Table I. Since we set estimation frequency to be 25Hz, the ratio "25" and "125" means the pause between each adjustment is 1 second and 5 seconds respectively. Besides, the ratio " ∞ " indicates we only adjust parameters once at the first step of estimation right after initialization.

TABLE IV
RMSE COMPARISON BETWEEN MODIFIED TEEs WITH DIFFERENT ADJUSTMENT FREQUENCIES (UNIT: M)

Period Ratio	B ₁	B ₂	B ₃	Y ₀	Y ₁	Y ₂	Y ₃
1	0.16	0.15	0.19	0.35	0.33	0.33	0.54
25	0.16	0.14	0.30	0.50	0.49	0.43	0.63
125	0.17	0.15	0.37	0.57	0.53	0.49	0.63
∞	0.17	0.15	0.42	0.63	0.50	0.58	0.64
N/A	0.16	0.16	0.47	0.71	0.48	0.41	0.62

From the results, we see original TEE outperforms all other tests for most of the time. In normal environments like B₁ and B₂, adjustment frequency doesn't affect estimation performance. And in harsh environments, the performance deteriorates as the pause time between each adjustment increases. Interestingly, the one that only adjusts ones and that doesn't adjust may sometimes performs better than those that adjust with pause. This is because keeping parameters unchanged through estimation provides additional stability. But this stability cannot offset lost adaptability. In general, TEE shows the best balance between accuracy and adaptability.

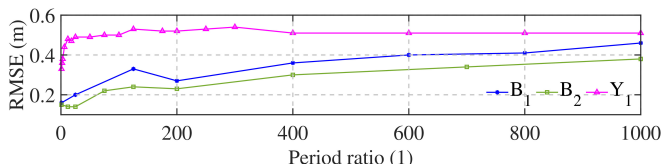


Fig. 12. Relation between estimation performance and adjustment period ratio, tested on dataset B₁, B₂ and Y₁.

We further conduct more tests to find relation between estimation performance and adjustment frequency. The results are plotted in Fig. 12. As ratio grows, RMSE first increases rapidly, which indicates the estimator is losing its adaptability. Soon after the pause is long enough, the slope gets near to zero and RMSE reaches its maximum. Eventually, the pause is considerable compared to total time and adjustment only happens several times. This slightly enhances stability instead and RMSE may get a little lower. More details of adaptability loss are shown in Fig. 13, where we consider reduced determinant (abbr. RedDet) ratio of noise covariance matrices, $\sqrt[6]{|Q|}/\sqrt[4]{|R|}$, as an indicator to compare performance of each estimator with different period ratio. The extent of each adjustment is limited owing to applied restrictions, which counts for the adaptability loss as period ratio grows. In harsh environments, its adaptability that plays an important role in

estimation performance. Hence it's necessary to conduct adaptive adjustment simultaneously together with state estimation.

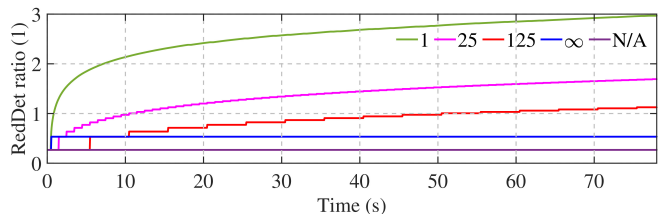


Fig. 13. Comparison of adaptability between estimators on dataset B₃ with different period ratio. The reduced determinant (abbr. RedDet) ratio, $\sqrt[6]{|Q|}/\sqrt[4]{|R|}$, is used as an indicator of adaptability.

VI. CONCLUSION

In this paper, we propose a ternary evolving estimator for UAV positioning in harsh environments, which simultaneously estimates the states, noise covariance matrices and aerial drag. We introduce an innovative error propagation matrix as an online inspector to assess estimation performance. Building upon this, we impose inherent restrictions to ensure proper evolution of the estimator and mitigate potential divergence caused by sensor malfunctions. Furthermore, we develop an adaptive aerial drag estimator to dynamically adjust the motion model, thereby enhancing overall performance. We also mathematically prove its observability, low numerical sensitivity and arithmetic efficiency. Numerous experiments validate the effectiveness of our estimator. Our proposed method achieves an average RMSE of 0.17m in common environments and 0.39m in harsh environments, significantly outperforms the state-of-the-art, especially in blinking and smoky environments. Moreover, Our sensor configuration and algorithm design exhibit in handling abrupt changes like sharp turns and sudden trajectory fluctuations. Additionally, we conduct ablation experiments by selectively removing parts of our method to verify necessity of inherent restrictions and effectiveness of aerial drag estimation. This underscores the critical role of each design and confirms our method's proficiency in harsh environments.

Moving forward, we aim to enhance the adaptability of our estimator in even more challenging scenarios. During experiments, we observed slight UAV trajectory and attitude vibrations stemming from a simplified controller, which will also be addressed in the future.

APPENDIX A PROOF TO LEMMA 1

Since \mathbf{X} conforms to matrix normal distribution $\mathbf{N}(\mathbf{0}, \mathbf{C})$, the PDF has the form:

$$\begin{aligned}
 p(\mathbf{X}|\mathbf{C}) &\propto |\mathbf{C}|^{\frac{K}{2}} \exp\left(-\frac{1}{2}\mathbf{X}^T\mathbf{C}^{-1}\mathbf{X}\right) \\
 &= |\mathbf{C}|^{\frac{K}{2}} \exp\left(-\frac{1}{2}\text{tr}\left(\mathbf{X}^T\mathbf{C}^{-1}\mathbf{X}\right)\right) \\
 &= |\mathbf{C}|^{\frac{K}{2}} \exp\left(-\frac{1}{2}\text{tr}\left(\mathbf{X}\mathbf{X}^T\mathbf{C}^{-1}\right)\right).
 \end{aligned}$$

We also know the prior PDF of C :

$$p(C) = \mathbf{IW}(C; \sigma, \Sigma) \propto |C|^{\frac{\sigma+n-1}{2}} \exp\left(-\frac{1}{2}\text{tr}(\Sigma C^{-1})\right).$$

According to Bayesian rule, the posterior PDF is:

$$\begin{aligned} p(C|\mathbf{X}) &\propto p(\mathbf{X}|C)p(C) \\ &\propto |C|^{\frac{\sigma+K+n-1}{2}} \exp\left(-\frac{1}{2}\text{tr}\left((\Sigma + \mathbf{X}\mathbf{X}^T)C^{-1}\right)\right) \\ &\propto \mathbf{IW}(C; \sigma + K, \Sigma + \mathbf{X}\mathbf{X}^T). \end{aligned}$$

By normalizing the above PDF, the proportional coefficient is obtained and the lemma is proved.

APPENDIX B PROOF TO LEMMA 2

Substitute $\hat{\mathbf{x}}_{f,0} = \bar{\mathbf{x}}_0 + \delta\mathbf{x}_0$ into (12) and (13), we have:

$$\begin{aligned} \tilde{\mathbf{x}}_{f,1} &= \mathbf{A}_0(\bar{\mathbf{x}}_0 + \delta\mathbf{x}_0) + \mathbf{u}_1 \triangleq \bar{\mathbf{x}}_1 + \mathbf{A}_0\delta\mathbf{x}_0 \\ \hat{\mathbf{x}}_{f,1} &= (\bar{\mathbf{x}}_1 + \mathbf{A}_0\delta\mathbf{x}_0) + \mathbf{K}_1(\tilde{\mathbf{y}}_1 - \tilde{\mathbf{C}}_1(\bar{\mathbf{x}}_1 + \mathbf{A}_0\delta\mathbf{x}_0)) \\ &= \bar{\mathbf{x}}_1 + (\mathbf{I}_6 - \mathbf{K}_1\tilde{\mathbf{C}}_1)\mathbf{A}_0\delta\mathbf{x}_0 \end{aligned}$$

which is $\delta\mathbf{x}_1 = (\mathbf{I}_6 - \mathbf{K}_1\tilde{\mathbf{C}}_1)\mathbf{A}_0\delta\mathbf{x}_0$. By iterating the above steps, the lemma is proved.

APPENDIX C DETAILS OF MATRICES IN THEOREM 1

$$\begin{cases} \mathbf{X}_0 = \mathbf{0}_3 \\ \mathbf{X}_1 = \mathbf{I}_3 \\ \mathbf{X}_2 = 2\mathbf{I}_3 - dt\boldsymbol{\mu} \\ \mathbf{X}_3 = 3\mathbf{I}_3 - 3dt\boldsymbol{\mu} + dt^2\boldsymbol{\mu}^2 \\ \mathbf{X}_4 = 4\mathbf{I}_3 - 6dt\boldsymbol{\mu} + 4dt^2\boldsymbol{\mu}^2 - dt^3\boldsymbol{\mu}^3 \\ \mathbf{X}_5 = 5\mathbf{I}_3 - 10dt\boldsymbol{\mu} + 10dt^2\boldsymbol{\mu}^2 - 5dt^3\boldsymbol{\mu}^3 + dt^4\boldsymbol{\mu}^4 \end{cases}$$

APPENDIX D PARAMETERS OF TEE IN EXPERIMENTS

On the left hand side are parameters for Algorithm 2 while on the right hand side are initial values for iteration.

Item	Value	Item	Value
k_w	10	$\boldsymbol{\mu}_0$	diag(0.2, 0.2, 0.8)
λ_0	1×10^{-3}	$\tilde{\mathbf{P}}_0$	$0.1 \cdot \mathbf{I}_6$
f_1	1×10^{-2}	$\tilde{\mathbf{x}}_0$	VICON ground truth
f_2	0.1	$\tilde{\boldsymbol{\Phi}}_0$	$17 \cdot \mathbf{I}_6$
b_u	1×10^{-2}	$\tilde{\phi}_0$	10
b_l	1×10^{-3}	$\tilde{\boldsymbol{\Psi}}_0$	$13 \cdot \mathbf{I}_4$
ε	1×10^3	$\tilde{\psi}_0$	8

REFERENCES

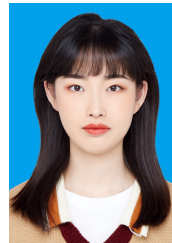
- [1] R. La Scalea, M. Rodrigues, D. P. M. Osorio, C. H. Lima, R. D. Souza, H. Alves, and K. C. Branco, "Opportunities for autonomous uav in harsh environments," in *2019 16th International Symposium on Wireless Communication Systems (ISWCS)*, 2019, pp. 227–232.
- [2] B. Peng, Y. Chen, T. Zheng, C. Duan, and Z. Yao, "Safety positioning for uav swarms in harsh environments," *IEEE Network*, vol. 36, no. 4, pp. 46–53, 2022.
- [3] K. Gao, H. Wang, H. Lv, and P. Gao, "A dl-based high-precision positioning method in challenging urban scenarios for b5g ccuavs," *IEEE Journal on Selected Areas in Communications*, vol. 41, no. 6, pp. 1670–1687, 2023.
- [4] A.-M. Drăgulescu, C. Zamfirescu, S. Halunga, I. Marcu, F. Y. Li, and O. A. Dobre, "Understanding lorawan transmissions in harsh environments: A measurement-based campaign through unmanned aerial/surface vehicles," *IEEE Transactions on Instrumentation and Measurement*, vol. 73, pp. 1–14, 2024.
- [5] L. Zhang, J. Chen, C. Wu, Q. Qie, and Y. Jin, "Uav path planning based on vision," in *2023 IEEE International Conference on Unmanned Systems (ICUS)*, 2023, pp. 7–10.
- [6] M. Rezinkina, O. Rezinkin, and A. Zaporozhets, "Uavs application in power engineering," in *2021 IEEE 6th International Conference on Actual Problems of Unmanned Aerial Vehicles Development (APUAVD)*, 2021, pp. 161–164.
- [7] Y. Gao and G. Li, "A gnss instrumentation covert directional spoofing algorithm for uav equipped with tightly-coupled gnss/imu," *IEEE Transactions on Instrumentation and Measurement*, vol. 72, pp. 1–13, 2023.
- [8] X. Zhou, Y. Chen, Y. Liu, and J. Hu, "A novel sensor fusion method based on invariant extended kalman filter for unmanned aerial vehicle," in *2021 IEEE International Conference on Robotics and Biomimetics (ROBIO)*, 2021, pp. 1111–1116.
- [9] J.-T. Zou, C.-Y. Wang, and Y. M. Wang, "The development of indoor positioning aerial robot based on motion capture system," in *2016 International Conference on Advanced Materials for Science and Engineering (ICAMSE)*, 2016, pp. 380–383.
- [10] T. Pavlenko, M. Schütz, M. Vossiek, T. Walter, and S. Montenegro, "Wireless local positioning system for controlled uav landing in gnss-denied environment," in *2019 IEEE 5th International Workshop on Metrology for AeroSpace (MetroAeroSpace)*, 2019, pp. 171–175.
- [11] Z. Wang, S. Liu, G. Chen, and W. Dong, "Robust visual positioning of the uav for the under bridge inspection with a ground guided vehicle," *IEEE Transactions on Instrumentation and Measurement*, vol. 71, pp. 1–10, 2022.
- [12] L. Ruan, G. Li, W. Dai, S. Tian, G. Fan, J. Wang, and X. Dai, "Cooperative relative localization for uav swarm in gnss-denied environment: A coalition formation game approach," *IEEE Internet of Things Journal*, vol. 9, no. 13, pp. 11 560–11 577, 2022.
- [13] A. Marut, P. Wojciechowski, K. Wojtowicz, and K. Falkowski, "Visual-based landing system of a multicopter uav in gnss denied environment," in *2023 IEEE 10th International Workshop on Metrology for AeroSpace (MetroAeroSpace)*, 2023, pp. 308–313.
- [14] Z. Jiang, J. Tan, D. Huang, and Y. Meng, "Robust visual positioning of the uav for the regional operation," in *2023 CAA Symposium on Fault Detection, Supervision and Safety for Technical Processes (SAFEPROCESS)*, 2023, pp. 1–5.
- [15] L. Yu, E. Yang, B. Yang, Z. Fei, and C. Niu, "A robust learned feature-based visual odometry system for uav pose estimation in challenging indoor environments," *IEEE Transactions on Instrumentation and Measurement*, vol. 72, pp. 1–11, 2023.
- [16] S. W. Chen, G. V. Nardari, E. S. Lee, C. Qu, X. Liu, R. A. F. Romero, and V. Kumar, "Sloam: Semantic lidar odometry and mapping for forest inventory," *IEEE Robotics and Automation Letters*, vol. 5, no. 2, pp. 612–619, 2020.
- [17] B. Yang, E. Yang, L. Yu, and A. Loeliger, "High-precision uwb-based localisation for uav in extremely confined environments," *IEEE Sensors Journal*, vol. 22, no. 1, pp. 1020–1029, 2022.
- [18] K.-H. Lin, H.-M. Chen, G.-J. Li, and S.-S. Huang, "Analysis and reduction of the localization error of the uwb indoor positioning system," in *2020 IEEE International Conference on Consumer Electronics - Taiwan (ICCE-Taiwan)*, 2020, pp. 1–2.
- [19] M. Fu, H. Zhang, S. Wang, and Y. Shui, "Rotating 3d laser mapping system for multi-rotor drones," in *2023 2nd International Conference on Robotics, Artificial Intelligence and Intelligent Control (RAIIC)*, 2023, pp. 1–6.
- [20] K. Li, S. Bu, Y. Dong, Y. Wang, X. Jia, and Z. Xia, "Uwb-vo: Ultra-wideband anchor assisted visual odometry," in *2023 IEEE International Conference on Unmanned Systems (ICUS)*, 2023, pp. 943–950.
- [21] Q. Zeng, H. Yu, X. Ji, X. Tao, and Y. Hu, "Fast and robust semidirect monocular visual-inertial odometry for uav," *IEEE Sensors Journal*, vol. 23, no. 20, pp. 25 254–25 262, 2023.
- [22] C. Papachristos, S. Khattak, and K. Alexis, "Autonomous exploration of visually-degraded environments using aerial robots," in *2017 International Conference on Unmanned Aircraft Systems (ICUAS)*, 2017, pp. 775–780.

- [23] T. Barfoot, *State Estimation for Robotics: Second Edition*. Cambridge University Press, 2024.
- [24] J. D. Schiller and M. A. Müller, “Suboptimal nonlinear moving horizon estimation,” *IEEE Transactions on Automatic Control*, vol. 68, no. 4, pp. 2199–2214, 2023.
- [25] C. Jiang, S. Zhang, H. Li, and Z. Li, “Performance evaluation of the filters with adaptive factor and fading factor for gnss/ins integrated systems,” *GPS Solutions*, vol. 25, no. 4, p. 130, Jul 2021. [Online]. Available: <https://doi.org/10.1007/s10291-021-01165-4>
- [26] Q. Pan, Y. Zhang, and Y. Liu, “Fuzzy adaptive extended kalman filter slam algorithm based on the improved pso algorithm,” in *2019 Chinese Automation Congress (CAC)*, 2019, pp. 3488–3493.
- [27] M. N. Ibarra-Bonilla, P. Jorge Escamilla-Ambrosio, J. Manuel Ramirez-Cortes, and C. Vianchada, “Pedestrian dead reckoning with attitude estimation using a fuzzy logic tuned adaptive kalman filter,” in *2013 IEEE 4th Latin American Symposium on Circuits and Systems (LASCAS)*, 2013, pp. 1–4.
- [28] A. Dey, “Adaptive cubature kalman filter for bearing only tracking with non-additive sensor noise,” in *2020 International Conference on Emerging Trends in Information Technology and Engineering (ic-ETITE)*, 2020, pp. 1–6.
- [29] C. Jiang, Z. Wang, H. Liang, and Y. Wang, “A novel adaptive noise covariance matrix estimation and filtering method: Application to multi-object tracking,” *IEEE Transactions on Intelligent Vehicles*, vol. 9, no. 1, pp. 626–641, 2024.
- [30] X. Wu, E. Zakeri, and W.-F. Xie, “Adaptive robust kalman filter for vision-based pose estimation of industrial robots,” in *2019 IEEE 5th International Conference on Computer and Communications (ICCC)*, 2019, pp. 298–302.
- [31] L. Jiang, W. Fu, H. Zhang, Z. Li, and L. Chi, “An improved robust adaptive kalman filtering algorithm,” in *2019 Chinese Control Conference (CCC)*, 2019, pp. 4167–4171.
- [32] S. Akhlaghi, N. Zhou, and Z. Huang, “Adaptive adjustment of noise covariance in kalman filter for dynamic state estimation,” in *2017 IEEE Power & Energy Society General Meeting*, 2017, pp. 1–5.
- [33] F. Zhu, Y. Huang, C. Xue, L. Mihaylova, and J. Chambers, “A sliding window variational outlier-robust kalman filter based on student’s t-noise modeling,” *IEEE Transactions on Aerospace and Electronic Systems*, vol. 58, no. 5, pp. 4835–4849, 2022.
- [34] Y. Huang, G. Jia, B. Chen, and Y. Zhang, “A new robust kalman filter with adaptive estimate of time-varying measurement bias,” *IEEE Signal Processing Letters*, vol. 27, pp. 700–704, 2020.
- [35] S. Qiao, Y. Fan, G. Wang, D. Mu, and Z. He, “Modified strong tracking slide window variational adaptive kalman filter with unknown noise statistics,” *IEEE Transactions on Industrial Informatics*, vol. 19, no. 8, pp. 8679–8690, 2023.
- [36] M. Vaishnavi and P. B. Bobba, “Extensive analysis on load dynamics of an unmanned aerial vehicle,” in *2019 IEEE 5th International Conference for Convergence in Technology (I2CT)*, 2019, pp. 1–6.
- [37] W. Dong, Z. Mei, Y. Ying, S. Chen, Y. ie, and X. Zhu, “Sribo: An efficient and resilient single-range and inertia based odometry for flying robots,” 2022. [Online]. Available: <https://arxiv.org/abs/2211.03093>
- [38] S. Chen, Y. Li, and W. Dong, “High-performance relative localization based on key-node seeking considering aerial drags using range and odometry measurements,” *IEEE Transactions on Industrial Electronics*, vol. 71, no. 6, pp. 6021–6031, 2024.
- [39] S. Zhujie, L. Fen, Z. Youqun, and M. Shougang, “Vehicle state and parameter estimation based on improved adaptive dual extended kalman filter with variable sliding window,” in *2022 6th CAA International Conference on Vehicular Control and Intelligence (CVCI)*, 2022, pp. 1–6.
- [40] N. van der Laan, M. Cohen, J. Arsenaault, and J. R. Forbes, “The invariant rauch-tung-striebel smoother,” *IEEE Robotics and Automation Letters*, vol. 5, no. 4, pp. 5067–5074, 2020.



Kaiwen Xiong is currently pursuing undergraduate degree in automation with Shanghai Jiao Tong University, Shanghai, China.

He is currently with the State Key Laboratory of Mechanical System and Vibration, School of Mechanical Engineering. His research interests include state estimation and adaptive positioning of unmanned systems.



Sijia Chen received the B.S. degree in mechanical design manufacture and automation from the University of Electronic Science and Technology of China, Sichuan, China, in 2022. She is currently a Ph.D. candidate with the State Key Laboratory of Mechanical System and Vibration, School of Mechanical Engineering, Shanghai Jiao Tong University.

Her research interests include state estimation and intelligent control of unmanned systems.



Wei Dong received the B.S. degree and Ph.D. degree in mechanical engineering from Shanghai Jiao Tong University, Shanghai, China, in 2009 and 2015, respectively.

He is currently an associate professor in the Robotic Institute, School of Mechanical Engineering, Shanghai Jiao Tong University. For years, his research group was champions in several nationwide autonomous navigation competitions of unmanned aerial vehicles in China. In 2022, he was selected into the Shanghai Rising-Star Program for distinguished young scientists. His research interests include cooperation, perception and agile control of unmanned systems.